Self-Similar Anisotropic Texture Analysis: The Hyperbolic Wavelet Transform Contribution

Stéphane G. Roux, Marianne Clausel, Béatrice Vedel, Stéphane Jaffard, and P. Abry, *Fellow, IEEE*

***Abstract*— Textures in images can often be well modeled using self-similar processes while they may simultaneously display anisotropy. The present contribution thus aims at studying jointly selfsimilarity and anisotropy by focusing on a specific classical class of Gaussian anisotropic selfsimilar processes. It will be first shown that accurate joint estimates of the anisotropy and selfsimilarity parameters are performed by replacing the standard 2D-discrete wavelet transform with the hyperbolic wavelet transform, which permits the use of different dilation factors along the horizontal and vertical axes. Defining anisotropy requires a reference direction that need not *a priori* match the horizontal and vertical axes according to which the images are digitized; this discrepancy defines a rotation angle. Second, we show that this rotation angle can be jointly estimated. Third, a nonparametric bootstrap based procedure is described, which provides confidence interval in addition to the estimates themselves and enables us to construct an isotropy test procedure, which can be applied to a single texture image. Fourth, the robustness and versatility of the proposed analysis are illustrated by being applied to a large variety of different isotropic and anisotropic self-similar fields. As an illustration, we show that a true anisotropy built-in self-similarity can be disentangled from an isotropic self-similarity to which an anisotropic trend has been superimposed.**

***Index Terms*— Self-similarity, anisotropy, gaussian fields, hyperbolic wavelet transform, scale invariance, rotation invariance, anisotropy test, bootstrap.**

I. INTRODUCTION

Texture classification. In numerous modern applications (satellite imagery [1], geography [2], biomedical imagery [3]–[7], geophysics [8], art investigation [9], …), the data available for analysis consist of images of homogeneous textures, that need to be characterized. Texture classification thus consists of classical problem in image processing that received considerable efforts in recent years (cf. e.g., [3], [10]–[16] and references therein).

Scale invariance and Self-similarity. Amongst the many different ways texture characterizations have been investigated, techniques based on *scale invariance*, or *fractal*, concepts are considered as promising, notably for the application fields listed above (cf. e.g., [17] for a review). Scale invariance can be defined as the fact that there exists no specific space-scale in data that play a preferred role in their space dynamic, or equivalently that all space-scales are equally important. Scale invariance in data implies that they are analyzed with (statistical) models that do not rely on the identification of specific scales (such as Markov models) but instead with models that aim at characterizing a relation amongst scales. Because *Self-Similarity* is a theoretically well-grounded, and relatively simple instance of scale invariance behaviors, it has often been proposed that Gaussian self-similar fields are relevant models enabling efficient characterization and classification of textures (cf. e.g, [15], [16]).

Anisotropy. However, textures are also often characterized by anisotropy, which may either be deeply tied to self-similarity itself [18], [19] or exist as an independent property that is superimposed to an isotropic self-similarity. In both cases, it is a crucial stake in analysis to disentangle self-similarity from anisotropy, to discriminate whether self-similarity and anisotropy are independent properties or if they are stemming from the same constructive mechanism, as well as to be able to estimate accurately the self-similarity parameter H, despite anisotropy. It has already been pointed out that fractal analysis and estimation is very sensitive to anisotropy (cf. e.g., [8]). In the literature, anisotropy is often analyzed from 1D slices extracted from images along different directions [6] or by making use of local directional differential estimators [20], [21].

Goals and contributions. In this context, elaborating on a preliminary attempt [22], the present contribution aims at proposing an efficient and elegant solution to the joint analysis and estimation of self-similarity and anisotropy in 2D fields. Though the procedure proposed here is designed for actual application to real-world textures, its performance are assessed by means of Monte Carlo simulation performed on synthetic isotropic and non isotropic Gaussian textures. While the (discrete) wavelet transform (DWT) is nowadays a classical tool for image processing, the key originality of the present work is to show that the classical discrete wavelet transform fails at providing a relevant analysis of self-similarity in presence of anisotropy. Instead, it is proposed here to replace the 2D Discrete Wavelet Transform with the *Hyperbolic Wavelet Transform* (HWT) (defined e.g., in [23]). Indeed, the use of dilation factors that differ along the x and y axes potentially

---

Manuscript received August 14, 2012; revised March 1, 2013 and June 22, 2013; accepted June 25, 2013. The associate editor coordinating the review of this manuscript and approving it for publication was Prof. Rebecca Willett.

S. G. Roux and P. Abry are with the Physics Department, ENS Lyon, CNRS, UMR5672, Lyon 69364, France (e-mail: stephane.roux@ens-lyon.fr; patrice.abry@ens-lyon.fr).

M. Clausel is with the Laboratoire Jean Kuntzmann, UMR 5224, University of Grenoble, Grenoble 38400, France (e-mail: marianne.clausel@imag.fr).

B. Vedel is with the LMBA, University of Bretagne Sud, European University of Bretagne, Vannes 56017, France (e-mail: beatrice.vedel@univ-ubs.fr).

S. Jaffard is with the University of Paris Est, LAMA, CNRS, UMR 8050, Créteil 94010, France (e-mail: jaffard@univ-paris12.fr).

Digital Object Identifier 10.1109/TIP.2013.2272515

permits to *see* the anisotropy, as opposed to the classical 2D Discrete Wavelet Transform relying on a single and isotropic dilation factor. The Hyperbolic Wavelet Transform is defined in Section II-B. Note that the HWT has appeared earlier in the literature under different names, such as *separable wavelet* [24], *Tensor-product wavelet* [25], *anisotropic wavelet transform* [26] or *rectangular wavelet transform* [27], without specific exploration though of its benefits to study anisotropy in textures. Also, redundant (or overcomplete) wavelet representations (such as M-band, dual tree and Hilbert pair complex wavelets, cf. e.g., [28], [29] for enlightening reviews) may be used to analyze images and textures. However, while they suffer from a larger computational cost, they have been observed (in preliminary attempts performed by the authors) to yield little, if not no, practical benefit for the study of scale invariance and the estimation of the corresponding parameters. Overcomplete wavelet representations are thus excluded from the present study.

As representative of 2D model mixing self-similarity and anisotropy, self-similar Gaussian 2D random fields with built-in anisotropy, such as those proposed in e.g., [18], [19], are used here. These fields are defined and illustrated in Section II-A and their hyperbolic wavelet analysis is detailed in Section II-C.

Estimation procedures for the parameters characterizing self-similarity and anisotropy are defined and their performance assessed in Section III-A. The definition of anisotropy involves a rigid definition of reference (orthogonal) axes, that have no a priori reason to match those of the sensor used to acquire the image and thus to coincide with the horizontal x and vertical y axis along which the image is presented for analysis. Therefore, the model introduced in Section II-A includes a rotation parameter that accounts for this unknown. An estimation procedure for this rotation is devised and analyzed in Section III-B. Therefore, the parameters characterizing rotation, anisotropy and self-similarity are estimated jointly.

For application purposes, it is crucial to be able to decide whether textures should be modeled by isotropic or anisotropic models. Therefore, a procedure for testing the null hypothesis that the texture is isotropic is constructed and studied in Section IV. It is based on a non parametric bootstrap procedure performed on the hyperbolic wavelet coefficients (in the spirit of the construction devised in [30]) and can thus be applied to each single analyzed texture independently. Incidentally, the bootstrap procedures also provide practitioners with confidence intervals for the estimates, a very important feature for practical purposes.

Finally, the analysis procedures proposed here are applied in Section V to a variety of isotropic and anisotropic fields that differ from the precise model used as a reference model (cf. Section II-A), hence illustrating the robustness and generality of the tools proposed here. Notably, it is shown that the proposed analysis enables to potentially distinguish between a truly anisotropic self-similar field and an isotropic self-similar field (with same self-similar parameter) to which directional, hence anisotropic, oscillations, with no relation to selfsimilarity, have been additively superimposed.

II. HYPERBOLIC WAVELET ANALYSIS OF ANISOTROPIC SELF-SIMILAR RANDOM FIELDS

A. Anisotropic Self-Similar Random Fields

1) Definition: Because of its generic and representative nature, it has been chosen to work with the class of anisotropic Gaussian self-similar fields, introduced in [18], [19], referred to as *Operator Scaling Gaussian Random Field* (**OSGRF**) which can be defined using the following harmonizable representation:

$$X_{f,E_0,H_0}(\underline{x}) = \int_{\mathbb{R}^2} (e^{i\langle \underline{x},\underline{\xi}\rangle} - 1) f(\underline{\xi})^{-(H_0+1)} d\widehat{W}(\underline{\xi}), \quad (1)$$

where $\underline{x} = (x_1, x_2)$, $\underline{\xi} = (\xi_1, \xi_2)$, E_0 is a matrix satisfying $\mathrm{Tr}(E_0) = 2$, f a E_0–homogeneous continuous positive function (hence satisfying the homogeneity relationship $f(a^{E_0}\underline{\xi}) = af(\underline{\xi})$ on $\mathbb{R}^2$) such that $\int(1 \wedge |\underline{\xi}|^2) f(\underline{\xi})^{-2(H_0+1)} d\underline{\xi} < +\infty$, and where $d\widehat{W}(\underline{\xi})$ stands for a 2D Wiener measure.

When f is not a radial function, the Gaussian field is not isotropic. In this study, it is chosen to use the following 2-parameter (related to anisotropy and rotation) explicit form:

$$f_{\theta_0,\alpha_0}(\underline{\xi}) = (|\zeta_1|^{1/\alpha_0} + |\zeta_2|^{1/(2-\alpha_0)}),$$

with $\underline{\zeta} = (\zeta_1, \zeta_2) = R_{\theta_0}\underline{\xi}$ and rotation matrix R_{θ_0} defined as:

$$R_{\theta_0} = \begin{pmatrix} \cos(\theta_0) & -\sin(\theta_0) \\ \sin(\theta_0) & \cos(\theta_0) \end{pmatrix}.$$

In this model,

$$E_0 = \begin{pmatrix} \alpha_0 & 0 \\ 0 & 2-\alpha_0 \end{pmatrix}, 0 < \alpha_0 < 2.$$

The rotation parameter θ_0 has been incorporated by ourselves into the original definition of [18], [19] to account for the fact that the rigid axes according to which anisotropy is defined need not match a priori the sensor axes according to which the image is digitalized (for real-world data) or numerically produced (for synthetic textures). In the sequel, **OSGRF** $X_{\theta_0,\alpha_0,H_0}$ thus refers to the following model, relying on 3 parameters, θ_0, α_0, H_0, characterizing respectively, rotation, anisotropy and self-similarity

$$X_{\theta_0,\alpha_0,H_0}(\underline{x}) = \int_{\mathbb{R}^2} (e^{i\langle \underline{x},\underline{\xi}\rangle} - 1) f_{\theta_0,\alpha_0}(\underline{\xi})^{-(H_0+1)} d\widehat{W}(\underline{\xi}) \quad (2)$$

2) Properties: With this construction, **OSGRF** $X_{\theta_0,\alpha_0,H_0}$ has stationary increments. It possesses a built-in anisotropy characterized by the parameter $\alpha_0 \in (0, 2)$. When $\alpha_0 = 1$, the field is isotropic and the case $1 < \alpha_0 < 2$ correspond to the case $0 < \alpha_0 < 1$ with the axes (x_1, x_2) permuted.

OSGRF $X_{\theta_0,\alpha_0,H_0}$ satisfies (where $\overset{\mathcal{L}}{=}$ denotes equality for all finite dimensional distributions):

$$\{X_{\theta_0,\alpha_0,H_0}(a^E\underline{x})\} \overset{\mathcal{L}}{=} \{a^{H_0} X_{\theta_0,\alpha_0,H_0}(\underline{x})\}. \quad (3)$$

with $E_0 = R_{\theta_0} E R_{-\theta_0}$. It is thus exactly self-similar with parameter $0 < H_0 < \min(\alpha_0, 2-\alpha_0) < 1$.

Fig. 1 displays realizations of $X_{\theta_0,\alpha_0,H_0}(\underline{x})$, obtained from MATLAB routines written by ourselves and available upon request. On top row, $(H_0, \theta_0) = (0.2, 0)$ are kept fixed while α_0 takes the values 1, 0.7 and 0.3 (from left to right). The practical goal is to estimate correctly H_0 despite these different

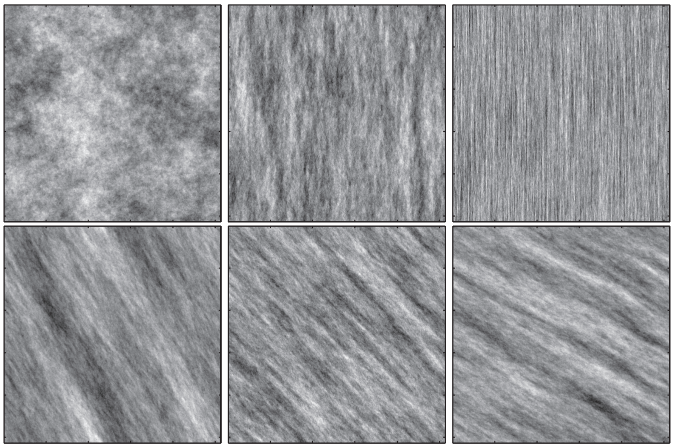

Fig. 1. **Sample fields of $X_{\theta_0,\alpha_0,H_0}$.** Top line : $(\theta_0, \alpha_0, H_0) = (0, \alpha_0, 0.2)$ with, from left to right $\alpha_0 = 1$ (isotropic); $\alpha_0 = 0.7$ and $\alpha_0 = 0.3$. Bottom line : $(\theta_0, \alpha_0, H_0) = (\theta_0, 0.7, 0.2)$ and, from left to right $\theta_0 = \pi/6$, $\theta_0 = \pi/4$ and $\theta_0 = \pi/3$.

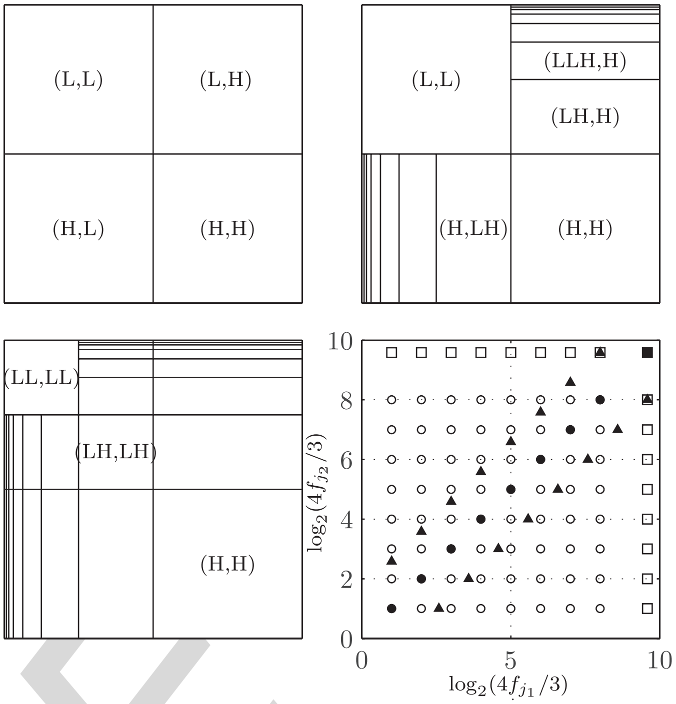

Fig. 2. **Hyperbolic Wavelet Transform.** Top line : one step of HWT consists of one step of 2D-DWT (left) (with 1D-DWT performed on each line of HL and each column of LH subbands (right)). Bottom line : second step of HWT (left) and locations of the HWT vs DWT (black dots) coefficients in the frequency domain (right). Black dots correspond to 2D-DWT while for HWT, white dots indicate subband HH, black triangles indicate LH and HL, squares correspond to the approximation coefficients). The circle symbols correspond to the coefficients ψ_{j_1,j_2} $j_1, j_2 \neq 0$ and square symbols to the coefficients $\psi_{0,j_2}, \psi_{j_1,0}, \psi_{0,0}$.

unknown anisotropy strengths α_0. On bottom row, a strongly anisotropic field is shown ($\alpha_0 = 0.3, H_0 = 0.2$) with three different rotation angles θ_0 (from left to right $\theta_0 = \pi/6$, $\pi/4$ and $\pi/3$). Here, the goal is to estimate correctly (α_0, H_0) despite such unknown rotation.

This three-parameter **OSGRF** stochastic process provides a rich and versatile model for selfsimilar (an)isotropic textures.

3) Numerical Simulation: Realizations (or sample fields) of the synthetic fields defined in Eq. (2) are produced numerically following the classical procedure, recalled in e.g., [19], relying on drawing at random realizations of white-noise $d\widehat{W}(\underline{\xi})$, followed by standard numerical integration procedures.

B. Hyperbolic Wavelet Transform

The 2D Hyperbolic Wavelet Transform (HWT) differs from the 2D Discrete Wavelet Transform (DWT) insofar as its definition relies on the use of two different dilation factors along the horizontal and vertical axes, as opposed to the 2D-DWT that makes use of a single and same dilation factor along both axes. This difference turns out to be crucial for the analysis of anisotropy.

The collection of functions constituting the orthogonal basis underlying the HWT is defined as tensor products of univariate wavelets (cf. e.g., [31]). Let φ and ψ denote the scaling function and the wavelet of a given one-dimensional multiresolution analysis. The HWT basis of $\mathcal{L}^2(\mathbb{R}^2)$ is defined as (cf. [23]):

$$\begin{aligned}
\psi_{j_1,j_2,k_1,k_2}(x_1,x_2) &= \psi(2^{j_1}x_1 - k_1)\psi(2^{j_2}x_2 - k_2),\\
\psi_{-1,j_2,k_1,k_2}(x_1,x_2) &= \varphi(x_1 - k_1)\psi(2^{j_2}x_2 - k_2),\\
\psi_{j_1,-1,k_1,k_2}(x_1,x_2) &= \psi(2^{j_1}x_1 - k_1)\varphi(x_2 - k_2),\\
\psi_{-1,-1,k_1,k_2}(x_1,x_2) &= \varphi(x_1 - k_1)\varphi(x_2 - k_2),
\end{aligned}$$

for all $\underline{j} = (j_1, j_2) \in \mathbb{N}^2$ and $\underline{k} = (k_1, k_2) \in \mathbb{Z}^2$. The HWT shares a deep relation with Triebel bases, used in mathematic literature, to characterize anisotropic functional spaces (cf. [32]).

The hyperbolic wavelet coefficients of the field X are defined, $\forall \underline{j} = (j_1, j_2) \in \mathbb{N}^2$, by :

$$d_X(\underline{j}, \underline{k}) = 2^{j_1+j_2} \int_{\mathbb{R}^2} \psi_{\underline{j},\underline{k}}(x_1, x_2) X(x_1, x_2) dx_1 dx_2. \qquad (4)$$

Note that a $\mathcal{L}^1$-normalization is used (instead of the classical $\mathcal{L}^2$-norm), as it better suits self-similarity analysis (cf. e.g., [33]). With these notations, fine resolution scales correspond to the limit $2^{j_1}, 2^{j_2} \to +\infty$, and index j in the decomposition corresponds to the actual resolution 2^{J-j}, where $J = \log_2(N)$, for an image of size $(N \times N)$.

Such coefficients $d_X(\underline{j}, \underline{k})$ can be computed efficiently, using a recursive pyramidal filter bank based algorithm comparable to that underlying the 2D-DWT. In Fig. 2, the first two iterations are illustrated, in the Fourier domain. One iteration of HWT practically consists of the combination of one iteration of the 2D-DWT algorithm, with 1D-DWT performed on each line of the vertical details (HL) and 1D DWT performed on each column of the horizontal details (LH). Because the central frequencies of the dilated scaling function of $\varphi(2^j x)$ and mother-wavelet $\psi(2^j x)$ can be approximated as $f_j = \frac{1}{4}2^j$ and $f_j = \frac{3}{4}2^j$, respectively, the HWT coefficients $d_X(\underline{j}, \underline{k})$ can be located in a (log-) frequency-frequency plane as shown in Fig. 2 bottom right, and thus compared to the location of the 2D-DWT coefficients.

In what follows, a 1D-Daubechies-3 multiresolution is used [34].

C. Analysis of Anisotropic Self-Similar Random Fields

From Eq. (4), the HWT coefficients can be rewritten, $\forall \underline{j} = (j_1, j_2) \in \mathbb{N}^{*2}$ and $\forall \underline{k} = (k_1, k_2) \in \mathbb{Z}^2$, as stochastic integrals:

$$d_X(\underline{j}, \underline{k}) = \int_{\mathbb{R}^2} \frac{\left(\prod_{\ell=1}^{2} e^{i2^{-j_\ell} k_\ell \xi_\ell} \overline{\widehat{\psi}(2^{-j_\ell} \xi_\ell)}\right)}{\left(|\xi_1|^{1/\alpha_0} + |\xi_2|^{1/(2-\alpha_0)}\right)^{H_0+1}} \, d\widehat{W}(\xi_1, \xi_2) \, . \tag{5}$$

Following the methodology in [35], [36], it can be proven that the HWT coefficients are weakly correlated, i.e., $\forall (j_1, j_2, k_1, k_2, k_1', k_2')$

$$\begin{aligned} &\left|\mathbb{E}(d_X((j_1, j_2), (k_1, k_2)) d_X((j_1, j_2), (k_1', k_2')))\right| \\ &\qquad \leq \frac{\mathbb{E}(|d_X((j_1, j_2, 0, 0)|^2)}{1 + |k_1 - k_1'| + |k_2 - k_2'|} \, . \end{aligned} \tag{6}$$

Using the substitution $\zeta_1 = 2^{-j_1}\xi_1$, $\zeta_2 = 2^{-j_2}\xi_2$ in the rewriting of definition of the wavelet coefficients (cf. Eq. (5)), we have been able to show that the HWT coefficients typically behave as [35], [36]:

$$d_X(\underline{j}, \underline{k}) \simeq 2^{\frac{j_1+j_2}{2}} \int_{\mathbb{R}^2} \frac{\left(\prod_{\ell=1}^{2} e^{ik_\ell \zeta_\ell} \overline{\widehat{\psi}(\zeta_\ell)}\right) d\widehat{W}(\zeta_1, \zeta_2)}{\left(2^{\frac{j_1}{\alpha_0}} |\zeta_1|^{\frac{1}{\alpha_0}} + 2^{\frac{j_2}{2-\alpha_0}} |\zeta_2|^{\frac{1}{2-\alpha_0}}\right)^{H_0+1}} \, ,$$

When $j_1/\alpha_0 > j_2/(2 - \alpha_0)$, we derive that, for all ζ_1, ζ_2:

$$\begin{aligned} 2^{\frac{j_1}{\alpha_0}} |\zeta_1|^{\frac{1}{\alpha_0}} &\leq 2^{\frac{j_1}{\alpha_0}} |\zeta_1|^{\frac{1}{\alpha_0}} + 2^{\frac{j_2}{2-\alpha_0}} |\zeta_2|^{\frac{1}{2-\alpha_0}} \\ &\leq 2^{\frac{j_1}{\alpha_0}} \left(|\zeta_1|^{\frac{1}{\alpha_0}} + |\zeta_2|^{\frac{1}{2-\alpha_0}}\right) \end{aligned}$$

and further

$$\begin{aligned} &2^{\frac{-j_1 H_0}{\alpha_0}} \frac{1}{(|\zeta_1|^{\frac{1}{\alpha_0}} + |\zeta_2|^{\frac{1}{2-\alpha_0}})^{H_0+1}} \\ &\quad \leq \frac{1}{2^{\frac{j_1}{\alpha_0}} |\zeta_1|^{\frac{1}{\alpha_0}} + 2^{\frac{j_2}{2-\alpha_0}} |\zeta_2|^{\frac{1}{2-\alpha_0}}} \leq 2^{\frac{-j_1 H_0}{\alpha_0}} \frac{1}{\left(|\zeta_1|^{\frac{H_0+1}{\alpha_0}}\right)} \end{aligned}$$

which enabled us to obtain the following inequality:

$$\begin{aligned} C_1 2^{\frac{j_1+j_2}{2}} 2^{-\frac{j_1(H_0+1)}{\alpha_0}} &\leq \mathbb{E}(|d_X(\underline{j}, \underline{k})|^2)^{1/2} \\ &\leq C_2 2^{\frac{j_1+j_2}{2}} 2^{-\frac{j_1(H_0+1)}{\alpha_0}} \, , \\ \text{with } C_1 &= \left(\int_{\mathbb{R}^2} \frac{\prod_{\ell=1}^{2} |\widehat{\psi}(\zeta_\ell)|^2 d\xi}{(|\zeta_1|^{\frac{1}{\alpha_0}} + |\zeta_2|^{\frac{1}{2-\alpha_0}})^{H_0+1}}\right)^{1/2} \, , \\ \text{and } C_2 &= \left(\int_{\mathbb{R}^2} \frac{\prod_{\ell=1}^{2} |\widehat{\psi}(\zeta_\ell)|^2 d\xi}{(|\zeta_1|^{\frac{H_0+1}{\alpha_0}})}\right)^{1/2} \, . \end{aligned}$$

Combined to similar arguments for the case $j_1/\alpha_0 \leq j_2/(2-\alpha_0)$, these computations enable us to show that the order of magnitude of the expectation of the squared HWT coefficients is, $\forall (j_1, j_2)$:

$$\mathbb{E}(|d_X(\underline{j}, \underline{k})|^2)^{1/2} \simeq 2^{\frac{j_1+j_2}{2}} 2^{-(H_0+1)\max(\frac{j_1}{\alpha_0}, \frac{j_2}{2-\alpha_0})}. \tag{7}$$

Because the fields we deal with are Gaussian, this can straightforwardly be extended to any $q \geq -2$, cf. [35]–[37]:

$$\mathbb{E}(|d_X(\underline{j}, \underline{k})|^q) \simeq 2^{q\frac{(j_1+j_2)}{2}} 2^{-q(H_0+1)\max(\frac{j_1}{\alpha_0}, \frac{j_2}{2-\alpha_0})}. \tag{8}$$

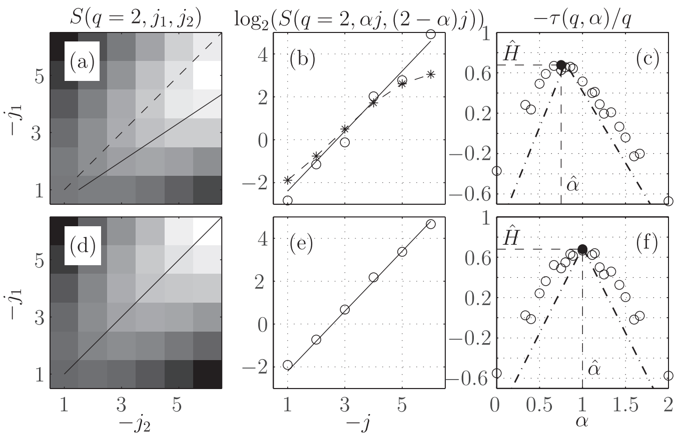

AQ:1

Fig. 3. **Illustrations of the estimation procedures.** For anisotropic, $\alpha_0 = 0.7$ (top row), and isotropic, $\alpha_0 = 1$ (bottom row), **OSGRF** $X_{\theta_0,\alpha_0,H_0}$, with $\theta_0 = 0$, $H_0 = 0.7$. Left column: Structure functions $S(q, j_1, j_2)$. The solid line indicates the direction $\hat{\alpha}$ while the dashed lines correspond to $\alpha = 1$ and hence the sole direction actually reachable with the coefficients of 2D-DWT. Middle column: Estimation of $H(\alpha)$, based on $\tau(q = 2, \alpha = \hat{\alpha})$ obtained from a linear regression of $\log_2 S(q, \alpha j, (2 - \alpha)j)$ versus j (∘). Solid lines correspond to the theoretical $-\tau(q = 2, \alpha_0)$. Stars (in (b)) correspond to the (biased) estimation of H from $-\tau(q = 2, \alpha = 1)$, i.e. by using only the 2D-DWT coefficients. Right column: Plots of $\hat{H}_2(\alpha) = -\tau(2, \alpha)/2$ versus α. The black dot shows the location of the maximum of $H_2(\alpha) = -\tau(2, \alpha)/2$ thus yielding the estimated $\hat{\alpha}$ and $\hat{H}$. In (f), as expected for an isotropic image, $\hat{\alpha} = 1$. The mixed line corresponds to the theoretical values of $-\tau(2, \alpha)/2$ (cf. Eq. 11).

These key results constitute the founding ingredient for the estimation procedures defined below.

III. PARAMETER ESTIMATION

The goal is now to define estimation procedures for the three-parameters entering the definition of **OSGRF** $X_{\theta_0,\alpha_0,H_0}$ and to study their statistical performance. It is assumed, first, that θ_0 is known and equal to $\theta_0 \equiv 0$ and estimation is devoted to parameters α_0 and H_0. In the second part, θ_0 is unknown and needs to be estimated as well. This is performed by applying the estimation of α_0 and H_0 to a collection of rotated images. It will be shown that the correct estimation angle is estimated when the estimation of the anisotropy coefficients reaches its minimum.

A. Self-Similarity and Anisotropy Parameters

In this section, θ_0 is assumed to be known and taken equal to 0 for simplicity.

1) Estimation Procedure: By analogy to what has classically been done for the analysis of self-similarity, or scale invariance in general, (cf. e.g., [38]), the space averages at joint scales (j_1, j_2) (also referred to as structure functions) are used as estimators for the ensemble averages appearing in Eq. (8) above:

$$S(q, j_1, j_2) = \frac{1}{n_{j_1,j_2}} \sum_{(k_1,k_2)\in\mathbb{Z}^2} |d_X(j_1, j_2, k_1, k_2)|^q, \tag{9}$$

where n_{j_1,j_2} stands for the number of available coefficients jointly at scales $(2^{j_1}, 2^{j_2})$.

Let us further define $\tau(q,\alpha)$ as a function of the statistical order $q > 0$ and of the anisotropy parameter α:

$$\tau(q,\alpha) = \liminf_{j} \frac{\log_2(S(q,\alpha j,(2-\alpha)j))}{j}. \qquad (10)$$

In essence, Eq. (10) amounts to assuming a power-law behavior of the structure functions with respect to scales, in the limit of fine scales $2^j \to +\infty$, along direction α:

$$S(q,\alpha j,(2-\alpha)j) \simeq S_0(q)2^{j\tau(q,\alpha)}.$$

Eq. (8) above indicates that, on average, and with the specific choice $(j_1,j_2) = (\alpha j,(2-\alpha)j)$:

$$S(q,\alpha j,(2-\alpha)j) \simeq 2^{jq\left(1-(H_0+1)\max(\frac{\alpha}{\alpha_0},\frac{2-\alpha}{2-\alpha_0})\right)}.$$

Comparing these two last relations suggests that $\tau(q,\alpha) = q\left(1-(H_0+1)\max(\frac{\alpha}{\alpha_0},\frac{2-\alpha}{2-\alpha_0})\right)$, so that, for a given fixed q, the anisotropy parameter α_0 can be estimated as:

$$\hat{\alpha}_{0,q} = \mathrm{argmin}_{\alpha}\,\tau(q,\alpha), \qquad (11)$$

and that the self-similarity parameter H can be estimated as:

$$\hat{H}_q = -\tau(q,\hat{\alpha}_{0,q})/q. \qquad (12)$$

2) Illustrations: The estimation procedure proposed here is sketched in Fig. 3, for $q = 2$, for an anisotropic (3a-c) and an isotropic (3d-e) **OSGRF** $X_{\theta_0,\alpha_0,H_0}$. It can be decomposed into three steps (for a given $q > 0$).

Step 1: The HWT coefficients $d_X(\underline{j},\underline{k})$ and corresponding structure functions $S(q,j_1,j_2)$ are computed. Examples are shown in Fig. 3 (left column).

Step 2: The surface $\log_2 S(q,j_1,j_2)$, seen as a function of the variables j_1, j_2 is interpolated (by nearest neighbor) along the line $\alpha j_1 + 1 = (2-\alpha)j_2 + 1$. Then, a non weighted least-square regression of $\log_2 S(q,\alpha j,(2-\alpha)j)$ versus $\log_2 2^j = j$ is performed across all available scales, hence yielding an estimate of $-\tau(q,\alpha)$, for each α and each q, as sketched in Fig. 3-b and 3-e).

Step 3: The estimated $-\tau(q,\alpha)$ are plotted for a given q, as a function of α, and its maximum yields the estimate $\hat{\alpha}$ of α_0 (cf. Fig. 3-c and 3-f). The estimation of the self–similarity parameter H_0 is further given by $\hat{H}_q = -\tau(q,\hat{\alpha})/q$.

This procedure calls for the following comments. First, Step 2 is performed for all accessible αs, that is, for all values of α, that connect at least two pairs of dyadic scales, i.e., $(a_1 = 2^{j_1}, a_2 = 2^{j_2})$ with integers $(j_1,j_2) = [1,2,\ldots,J]^2$. Therefore, the actual resolution of the values of α that can actually be used depends on the size $N \times N$ of the analyzed image, and hence so does the resolution of the estimate of the anisotropy parameter. This discretized resolution can be observed in Fig. 7.

Second, the structure functions $S(q,j,j)$ (hence for $\alpha = 1$) are computed from HWT coefficients that actually correspond to those of the 2D-DWT (cf. Fig. 3-b, dashed line). For isotropic fields, it is found that $\hat{\alpha} = 1$, and thus that the coefficients of the HWT that need to be actually used for the estimate of H_0 are those of the 2D-DWT. Conversely, for anisotropic fields, basing the estimate of H on $S(q,j,j)$ results into significant biases, as illustrated in Fig. 3-b, dashed line and Fig. 3-e, where the estimate of H_0 for $\alpha \equiv 1$ significantly differs from that obtained for $\alpha = \hat{\alpha}$. This illustrates the major benefits of replacing the 2D-DWT with the 2D-HWT.

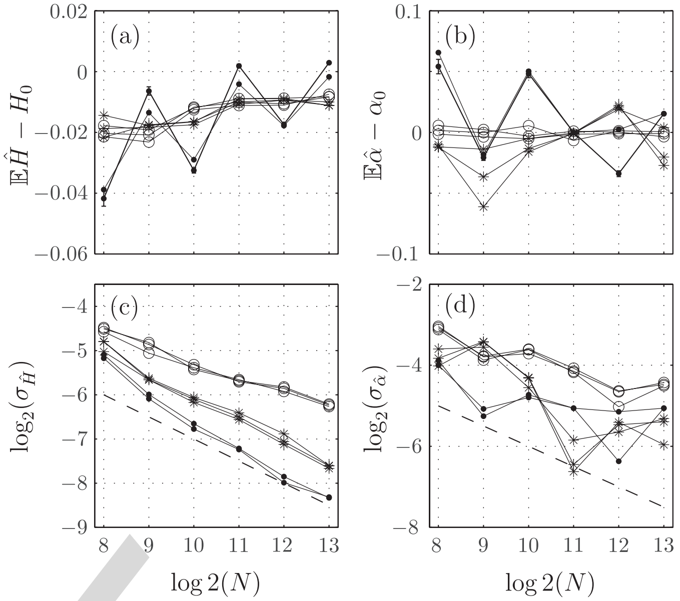

Fig. 4. **Estimation performance.** As functions of the sample size N (image size $N \times N$), biases (top row) and standard deviation for $\hat{H}_{q=2}$ (left column) and $\hat{\alpha}_{q=2}$ (right column), obtained as average of estimation performed on 500 realizations of **OSGRF** X_{0,α_0,H_0} with parameters $\alpha_0 = 1$, $H_0 = 0.7, 0.5$ and 0.3 (∘), $\alpha_0 = 0.8$, $H_0 = 0.7, 0.5, 0.3$ (∗) and $\alpha_0 = 0.6$, $H_0 = 0.5, 0.3$ (·). Bottom row, dashed lines illustrates the expected $1/sqrtN \times N$ decrease of the standard deviations.

3) Estimation Performance: To complement the theoretical study reported above and to further assess the performance of the proposed estimation procedures, Monte Carlo simulations are now performed further expanding on numerical investigations presented in [22]. Biases and the standard deviations of $\hat{\alpha}_q$ and $\hat{H}_q$ are obtained from averages of estimates computed over 500 independent realizations of **OSGRF** X_{0,α_0,H_0}, numerically produced by MATLAB routines designed by ourselves and available upon request.

Fig. 4 reports biases and standard deviations as a function of (the $\log_2$ of) the sample size N (image size is $N \times N$), for various parameters (α_0, H_0). Fig. 4 essentially shows that the estimation performance both for $\hat{\alpha}$ and $\hat{H}$ does not depend on H_0, a result that is highly reminiscent of the $1D$ case (cf. e.g., [39]). However, dependences on the anisotropy parameter α_0 do exist and are clearly visible on the standard deviation, which unexpectedly decrease with significant departures of isotropy.

Estimates are found to be asymptotically unbiased, as expected from theoretical analysis, and standard deviations roughly decrease as $1/\sqrt(N \times N) = 1/N$, in agreement with the weak correlation property of the HWT coefficients. Using other values of $q > 0$ (ranging from 1 to 5) yields similar conclusions.

To conclude this section, let us put the emphasis on the fact that image sizes vary from small ($2^8 \times 2^8$) to (very) large ($2^{13} \times 2^{13}$). This illustrates that both the synthesis and analysis procedures corresponding to the definition of **OSGRF**

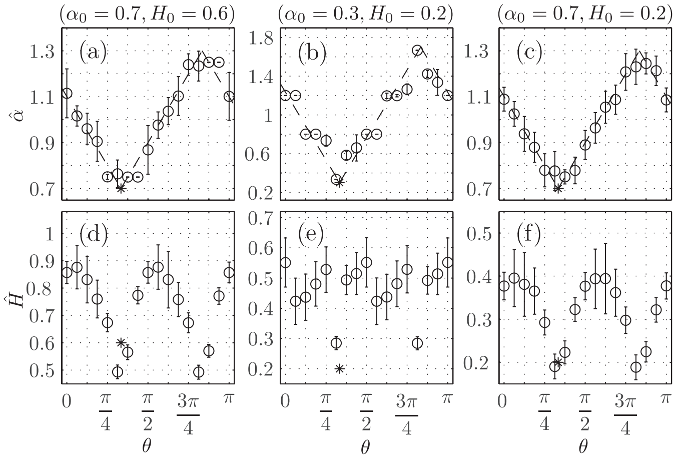

Fig. 5. **Joint three parameter estimation procedure.** Estimations of $\hat{\alpha}$ (top row) and $\hat{H}$ (bottom row) for three differents fields with $\theta_0 = \pi/3$ and $(\alpha_0, H_0) = (0.7, 0.6)$ ((a) and (d)); $(\alpha_0, H_0) = (0.3, 0.2)$ ((b) and (e)); $(\alpha_0, H_0) = (0.7, 0.2)$ ((c) and (f)). The dashed line illustrates the expected theoretical behavior of $\hat{\alpha}$ as a function of θ and the 'circle' with confidence intervals to Monte Carlo averages. The estimation of $\hat{\theta}$ corresponds to the location of the minimum of $\hat{\alpha}(\theta)$ and satisfactorily corresponds to $\theta_0 = \pi/3$. Final estimates for α_0 and H_0 are obtained as $\hat{\alpha}^* = \hat{\alpha}(\hat{\theta})$ and $\hat{H}^* = \hat{H}(\hat{\theta})$ and thus show satisfactory agreement with the theoretical values, marked by $*$. Error bars correspond to $\sigma_{\hat{H}}$ (resp. $\sigma_{\hat{\alpha}}$).

and its analysis can be implemented efficiently and benefits from a remarkably low computational cost.

Estimation performance were reported here only for $q = 2$, as it was found empirically that the use of other values of q did not improve performance, as can be expected for Gaussian fields.

B. Rotation Parameter

1) Estimation Procedure: Let us now consider the case where, in addition to H_0 and α_0, the rotation angle θ_0 is unknown. To estimate jointly the three unknown parameters, it is here proposed to apply the above procedure to estimate H_0 and α_0 to a collection of rotated versions of the original image, with rotation angles θ. The estimation of the anisotropy direction relies on the following observations, illustrated in Fig. 5 (top row): i) The estimate $\hat{\alpha}(\theta)$ is a π-periodic function; ii) it also has the symmetry $\hat{\alpha}(\theta_0 + \theta) = \hat{\alpha}(\theta_0 - \theta)$; iii) when $\theta = \theta_0$, $\hat{\alpha} \simeq \alpha$; iv) when $\theta = \theta_0 + \pi/2$, $\hat{\alpha} = 2 - \alpha$; v) and when $\theta = \theta_0 + \pi/4$, $\hat{\alpha} = 1$. Thus, the following joint estimation procedure for $(\theta_0, \alpha_0, H_0)$ can be proposed:

$$\hat{\theta} = \text{argmin}_\theta \hat{\alpha}(\theta), \tag{13}$$

$$\hat{\alpha}^* = \hat{\alpha}(\hat{\theta}) \tag{14}$$

$$\hat{H}^*_q = \hat{H}_q(\hat{\alpha}(\hat{\theta})). \tag{15}$$

Because the minimum of $\hat{\alpha}(\theta)$ is (arbitrarily) picked, this procedure necessarily implies $\hat{\alpha}^* \leq 1$, there is thus a remaining indetermination whether the correct choice is $\hat{\alpha}^*$ or $2 - \hat{\alpha}^*$ and therefore of $\pi/2$ in θ_0. As previously mentioned, this only amounts to exchanging the roles of the axis x and y. For isotropic fields, $\hat{\alpha}(\theta)$ fluctuates around $\alpha = 1$, and no clear minimum (or maximum) is visible. Furthermore, $\hat{\theta}_{max} - \hat{\theta}_{min}$ differs from $\pi/2$. When $\hat{\theta}_{max} - \hat{\theta}_{min} < \pi/4$, the field is thus declared isotropic and we set $\hat{\theta} = 0$.

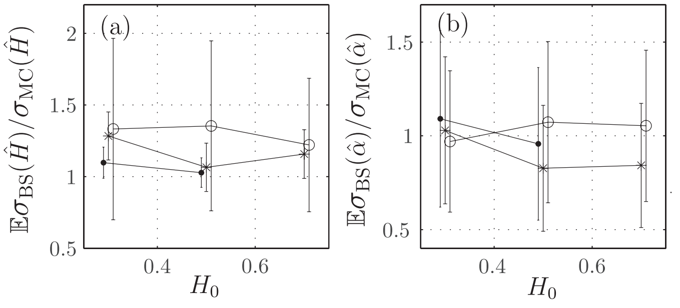

Fig. 6. **Bootstrap versus Monte Carlo Estimates of standard deviations.** (a) Estimations of $\mathbb{E}\sigma_{\text{BS}}(\hat{H})/\sigma_{\text{MC}}(\hat{H})$ as a function of H_0, for $q = 2$, obtained from $R = 100$ bootstraps applied to 100 independent copies of **OSGRF** X_{0,α_0,H_0} (image size $(2^{10}, 2^{10})$), with parameters $\alpha_0 = 1$ ($\circ$), $\alpha_0 = 0.8$ ($*$) and $\alpha_0 = 0.6$ ($\cdot$). (b) Estimations of $\mathbb{E}\sigma_{\text{BS}}(\hat{\alpha})/\sigma_{\text{MC}}(\hat{\alpha})$ as a function of H_0, for $\alpha_0 = 1$ ($\circ$), $\alpha_0 = 0.8$ ($*$) and $\alpha_0 = 0.6$ ($\cdot$).

To practically perform the rotation of θ on the image of analysis, a nearest neighbor interpolation is applied. The procedure is totally automated and no human supervision is needed.

2) Illustrations and Performance: To assess the performance of the joint three-parameter estimate procedure, Monte Carlo numerical simulations are conducted, and biases and standard deviations are computed from average over 100 realizations of **OSGRF** $X_{\theta_0,\alpha_0,H_0}$, for various choices of $(\theta_0, \alpha_0, H_0)$, and with $q = 2$.

Fig. 5 shows, top row, that the estimation $\hat{\alpha}(\theta)$ clearly follows a piecewise linear variation along θ (modeled by the dashed line) and displays clear extrema for $\theta \simeq \theta_0$ and $\theta \simeq \theta_0 + \pi/2$. For $\theta \simeq \theta_0$, $\hat{\alpha}(\hat{\theta})$ and $\hat{H}(\hat{\theta})$ (bottom line of Fig. 5) provide satisfactory estimates of α_0 and H_0. For $\theta = \hat{\theta} + \pi/2$, the estimations are $2 - \hat{\alpha}$ and $\hat{H}$. Table I displays the biases, standard deviations and mean square errors for several isotropic and anisotropic **OSGRF** $X_{\theta_0,\alpha_0,H_0}$ fields. It can be observed that $\hat{H}$ shows more bias when a rotation of the original image is performed. This is likely due to the interpolation procedure that smoothes out data and thus that *distorts* self-similarity and thus scale invariance at the finest scales. Better estimations for H can be achieved by discarding a few of the finest scales from the linear regression, when image size permits.

IV. BOOTSTRAP-BASED ANISOTROPY TEST AND CONFIDENCE INTERVALS

In applications, it is often of crucial importance to be able to test the isotropy assumption (i.e., whether $\alpha_0 = 1$ or not) for each single image independently. This theoretically requires the knowledge of the distribution of $\hat{\alpha}$. Though it is found empirically Gaussian, the variance of the distribution remains unknown and, as suggested in Section III-A and Fig. 4, it depends not only on the sample size N but also on the unknown parameter α_0 itself. Asymptotic Gaussian expansions for the computations of the theoretical variance of $\hat{\alpha}$, in the spirit of those proposed for fractional Brownian motion in e.g., [40], have been observed to perform poorly (not reported here). Instead, it is proposed to apply non parametric bootstrap procedure in the HWT coefficient domain, in the spirit of the procedures developed and assessed in [30], [41]–[43]. This procedure is detailed in the next section while the corresponding bootstrapped based isotropy test is defined and assessed in Section IV-C.

A. Bootstrap Resampling Schemes

In a nutshell, nonparametric bootstrap makes use of available samples, many times, by a drawing with replacement procedure, to yield an approximation of the unknown population distribution. In turn, this estimated population distribution is used to construct confidence intervals or test (cf., e.g., [44] and [45]).

For the present work, following [30], the resampling procedure is applied in the HWT coefficient domain. Because HWT coefficients do not consist of independent random variables, but possess a residual correlation, a time-block bootstrap procedure is used: At each octave $\underline{j}$, block of size l of HWT coefficients are drawn randomly with replacement. This yields a set of bootstrapped HWT coefficients $d^*_X(\underline{j}, \underline{k})$, from which bootstrap estimates $\hat{\alpha}^*$ and $\hat{H}^*$ of α_0 and H_0, respectively, are obtained.

This procedure is repeated R times, and the population distribution of $\hat{\alpha}$ and $\hat{H}$ are inferred from the boostrap estimates $\hat{\alpha}^{*,r}$ and $\hat{H}^{*,r}$, $r = 1, \ldots, R$, notably variances can be estimated.

B. Bootstrap-Based Estimates of Variance

It has been found empirically that l need not depend on octave $\underline{j}$ and can be kept small. As documented in [30], l is set to twice the size of the support of the mother wavelet (e.g., for a Daubechies3 wavelet used here $l = 6$), as correlations amongst HWT coefficients is found to remain significant essentially over a space-scale controlled by the size of the wavelet support.

Fig. 6 compares the standard deviations of $\hat{H}$ (left) and $\hat{\alpha}$ obtained from 100 Monte Carlo simulations for anisotropic fields (of size $2^{10} \times 2^{10}$) against those obtained by the bootstrap procedure (with $R = 100$ for each of the 100 Monte Carlo simulations). Fig. 6 shows that the ratios $\sigma_{\text{BS}}(\hat{H})/\sigma_{\text{MC}}(\hat{H})$ and $\sigma_{\text{BS}}(\hat{\alpha})/\sigma_{\text{MC}}(\hat{\alpha})$ depend neither on α_0 nor on H_0 and remain close to 1, with a slight overestimation (from 10 to 20%) for the former and quasi perfect match for the latter. Equivalent conclusions are drawn from different sample sizes N. These results indicate that the bootstrap estimates of the variances provide valuable approximations of the true variances of $\hat{H}$ and $\hat{\alpha}$. Together with the Gaussian distribution empirical fact, this yields very satisfactory confidence intervals for $\hat{H}$ and $\hat{\alpha}$.

C. Test Procedure and Performance

1) Test Procedure: To test isotropy in a given image, the null and alternative hypothesis respectively read:

$$\mathcal{H}_0 : \alpha_0 - 1 = 0, \quad \text{and } \mathcal{H}_A : \alpha_0 - 1 \neq 0. \tag{16}$$

Let us assume first that $\theta_0 \equiv 0$. The test procedure can be decomposed as follows:

- Estimate $\hat{\alpha}$, as proposed in Section III-A.
- Apply the resampling scheme described in Section IV-A above to the HWT coefficients of $X_{\theta_0,\alpha_0,H_0}$ and construct the bootstrap distribution estimate of $\hat{\alpha}$ from the boostrap estimates $\hat{\alpha}^{*,r}$, $r = 1, \ldots R$.
- Set the test significance level δ for the test.
- Because when $\theta_0 \equiv 0$, there is no reason to decide a priori that the true α_0 will depart from 1 by being larger or smaller, a bilateral symmetric test is constructed. Assuming a normal distribution for $\hat{\alpha}$, the bootstrap-based standard deviation estimation σ^* is used to construct the equi-tailed and symmetric acceptance region $[-t_{\delta/2}\sigma^*, t_{\delta/2}\sigma^*]$, where $t_{\delta/2}$ denotes the $\delta/2$-th quantile of the zero-mean unit variance Gaussian distribution.
- Alternatively, the p-value of the test can be measured as the minimum between $P(\hat{\alpha}^* < \hat{\alpha}(\hat{\theta}))$ and $1 - P(\hat{\alpha}^* > \hat{\alpha}(\hat{\theta}))$, divided by 2.

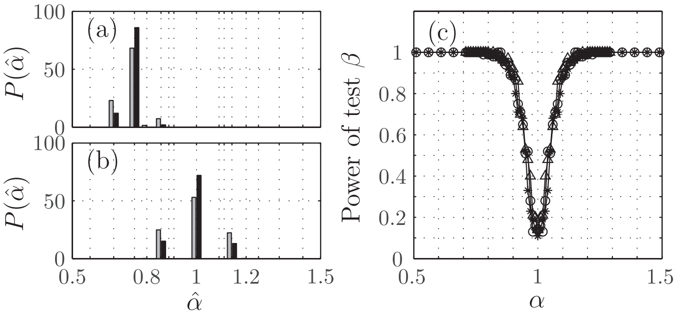

Fig. 7. **Anisotropy test**. a) Histogram of $\hat{\alpha}_{\text{MC}}$ (light gray) and of $\hat{\alpha}_{\text{BS}}$ (black) for **OSGRF** X_{0,α_0,H_0} (image size $(2^{10}, 2^{10})$), with $\alpha_0 = 0.75$ (a) and $\alpha_0 = 1$ (b). Right plot (c) shows the rejection level of the test (with a significance level of 90%) obtained for $R = 100$ bootstraps, averaged on 100 realizations of X_{0,α_0,H_0}, with $H_0 = 0.3$ (○), 0.5 (△) and 0.7 (▽).

2) Test Performance: To assess the validity and performance of the proposed test, it has been compared against Monte Carlo simulations, based on 100 independent copies of **OSGRF** $X_{\theta_0=0,\alpha_0,H_0}$ with various parameter settings and for image size $2^{10} \times 2^{10}$. Fig. 7a) and 7b) compare the histograms of the estimates of α_0 stemming from Monte Carlo simulations against those obtained from bootstrap estimates $\hat{\alpha}^*$, from a single realization, chosen arbitrarily, for anisotropic (a) and isotropic (b) fields. For both cases, distributions are found to be in satisfactory agreement. These figures also show that $\hat{\alpha}$ can only take discretized values, because of the finite sample size of the image, as discussed in Section III-A2.

In Fig. 7-c, the significance level of the test has been arbitrarily set to $\delta = 0.9$ and the rejection level of the bootstrap test ($R = 100$) has been computed as average over 100 independant Monte Carlo realizations of **OSGRF** $X_{\theta_0=0,\alpha_0,H_0}$ for various parameter settings. When $\alpha_0 = 1$, **OSGRF** is isotropic and the rejection level β is, as expected, found to satisfactorily reproduce the prescribed significance level $1 - \delta = 0.1$: $\hat{\beta} = 0.13$, 0.15 and 0.12 respectively for $H_0 = 0.7, 0.5$ and 0.3. When $\alpha_0 \neq 1$, **OSGRF** is anisotropic and the rejection level β measures the power of the test. Interestingly, it is found that the estimated power does not depend on H_0, is symmetric for α_0 above and below 1 and mostly that it increases sharply when α_0 departs from 1.

TABLE I

BIASES, STANDARD DEVIATIONS AND MEAN SQUARE ERRORS OBTAINED FROM 100 INDEPENDENT COPIES OF **OSGRF** $X_{\theta_0,\alpha_0,H_0}$ (IMAGE SIZE $(2^{10}, 2^{10})$). THE RIGHT COLUMN REPORTS THE CORRESPONDING REJECTION RATE OF THE ANISOTROPY TEST DESCRIBED IN SECTION IV-C3, WITH $R = 100$ BOOTSTRAP SURROGATES. THE SIGNIFICANCE LEVEL IS SET TO $1 - \delta = 10\%$

$(\theta_0, \alpha_0, H_0)$	$\langle\hat{\theta}\rangle - \theta_0$ (std,MSE)	$\langle\hat{\alpha}\rangle - \alpha_0$ (std,MSE)	$\langle\hat{H}\rangle - H_0$ (std,MSE)	% rej.
$(\pi/3, 0.7, 0.6)$	0.01 (0.03,0.00)	0.00 (0.04,0.00)	-0.10 (0.02,0.01)	100
$(\pi/3, 0.7, 0.2)$	0.01 (0.03,0.00)	0.01 (0.04,0.00)	-0.05 (0.02,0.00)	100
$(\pi/3, 0.3, 0.2)$	-0.01 (0.02,0.00)	0.01 (0.05,0.00)	-0.09 (0.09,0.02)	100
$(0, 1, 0.6)$	0.07 (0.31,0.01)	0.00 (0.08,0.01)	-0.01 (0.03,0.00)	8
$(0, 1, 0.2)$	0.08 (0.25,0.01)	-0.01 (0.08,0.01)	-0.01 (0.03,0.00)	11

This is thus indicating a strong potential to detect anisotropy even for small departure of α_0 from 1.

3) Test Procedure for $\theta_0 \neq 0$: When θ_0 is unknown and needs to be estimated, the procedure to test isotropy must be slightly amended, as follows:

- Apply estimation procedure for θ_0, α_0, H_0 as in Section III-B.
- For $\hat{\theta}$, store the estimate $\hat{\alpha}(\hat{\theta})$ and the rotated field $\tilde{X}_{\hat{\theta}}$.
- Apply the resampling scheme described in Section IV-A above to the HWT coefficients of $\tilde{X}_{\hat{\theta}}$ and construct the bootstrap distribution estimate of $\hat{\alpha}$ from the boostrap estimates $\hat{\alpha}^{*,r}, r = 1, \dots R$.
- Set the test significance level δ for the test.
- Because the estimated $\hat{\alpha}$ necessarily takes values in $[0, 1]$ a monolateral test must be constructed and the acceptance region is thus defined as: $[-t_\delta \sigma^*, 1]$.
- Alternatively, the p-value of the test can be computed as $P(\hat{\alpha}^* < \hat{\alpha}(\hat{\theta}))$.

Table I (right column) reports the rejection rates of the procedure applied to several anisotropic and isotropic **OSGRF** $X_{\theta_0,\alpha_0,H_0}$ fields of size $(2^{10}, 2^{10})$. For isotropic cases, the rejection rates matches closely the significance level, as expected. For anisotropic fields, the power of the test is found very high as soon as α_0 departs, even slightly, from 1.

V. OTHER ISOTROPIC AND ANISOTOPIC RANDOM FIELDS

So far, the analysis (estimation and test) procedures proposed here were applied only to the **OSGRF** $X_{\theta_0,\alpha_0,H_0}$, defined in Section II-A, and chosen as a convenient reference model, with three parameters accounting jointly for rotation, (an)isotropy and self-similarity. However, one can naturally wonder whether the isotropy test described above would satisfactorily perform to detect anisotropy for other models, i.e., whether $\hat{\alpha} = 1$ or not. In this section, a number of isotropic and non isotropic self-similar models commonly encountered in the image processing and statistics literature are used to test the level of generality of the approach proposed here.

TABLE II

Isotropie test: Rejection rates. OBTAINED FOR THREE DIFFERENT CLASSES OF FIELDS (FROM $R = 100$ BOOTSTRAPS ON EACH OF THE 100 1024×1024 REALIZATIONS, SIGNIFICANCE LEVEL OF $\delta = 90\%$)

H_1	0.7			0.4		
H_2	0.5	0.6	0.7	0.2	0.3	0.4
OSGRF	100	84	15	100	99	7
EFBF	42	31	15	49	28	10
FBS	89	78	58	92	87	61

A. Random Fields

1) Another OSGRF: In [46], another interesting instance of **OSGRF** has been explored. It is defined from Eq. (1) with:

$$f(\underline{\xi}) = (|\xi_1|^2 + |\xi_2|^{2a})^{-\beta}, \tag{17}$$

where $\beta = H_1 + (1 + 1/a)/2$ and $a = H_2/H_1$ for $0 < H_1 < H_2 < 1$. This process resembles **OSGRF** $X_{\theta_0,\alpha_0,H_0}$, in Eq. (2), with $\alpha_0 = 2a/(1 + a)$, $H_0 = 2aH_1/(1 + a)$ and $\theta_0 = 0$. It is thus anisotropic as soon as $a \neq 1$.

2) Extended Fractional Brownian Fields: Another class of possibly anisotropic Gaussian fields, referred to as *Extended Fractional Brownian Fields*, was first introduced in [18]. Its definition, $X_f(\underline{x}) = \int_{\mathbb{R}^2} (e^{i\langle \underline{x}, \underline{\xi}\rangle} - 1) f(\underline{\xi})^{1/2} d\widehat{W}(\underline{\xi})$, relies on an admissible function f of the form:

$$f(\underline{\xi}) = |\underline{\xi}|^{-2h(arg(\underline{\xi}))-2}, \tag{18}$$

where $arg(\underline{\xi})$ is the direction of the frequency $\underline{\xi}$ and h an even, measurable, periodic function taking values in $(0, 1)$. Fractional Brownian field is a particular and isotropic case of **EFBF**, where h is a constant function, but **EFBF**, is in general anisotropic when h is not a constant function. Strictly speaking, **EFBF** is not exactly selfsimilar (except in cases where h is a constant function). However, **EFBF** shows scale invariance properties that are empirically close to those of strictly selfsimilar fields. Fig. 8-a shows a sample field of anisotropic **EFBF**, with

$$h(arg(\underline{\xi})) = H_2 \times (\cos(2 \times arg(\underline{\xi})) + \epsilon)^2/(1 + \epsilon)^2, \tag{19}$$

where $\epsilon = 1 + 2\sqrt{H_1/(H_2 - H_1)}$. Function h is π-periodic and takes values in $[H_1, H_2]$. Fig. 8-c shows one sample-field, obtained with parameters $H_1 = 0.2$ and $H_2 = 0.8$.

3) Fractional Brownian Sheet: Fractional Brownian Sheet (**FBS**), introduced in [47], provides another class of (an)isotropic self-similar Gaussian field. It can be defined through its harmonizable representation, for any (H_1, H_2) in $(0, 1)^2$ (see [48]) :

$$B_{H_1,H_2}(x) = \int_{\mathbb{R}^2} \frac{(e^{i<x_1,\xi_1>} - 1)(e^{i<x_2,\xi_2>} - 1)}{|\xi_1|^{H_1+\frac{1}{2}} |\xi_2|^{H_2+\frac{1}{2}}} d\widehat{W}_{\xi_1,\xi_2}, \tag{20}$$

where dW_{x_1,x_2} is a Brownian measure on $\mathbb{R}^2$ and $d\widehat{W}_{\xi_1,\xi_2}$ its Fourier transform. **FBS** is a Gaussian field with stationary rectangular increments, satisfying the following scaling property $\forall (a_1, a_2) \in (\mathbb{R}_+^*)^2$

$$\{B_{H_1,H_2}(a_1 x_1, a_2 x_2)\} \overset{\mathcal{L}}{=} \{a_1^{H_1} a_2^{H_2} B_{H_1,H_2}(x_1, x_2)\} . \tag{21}$$

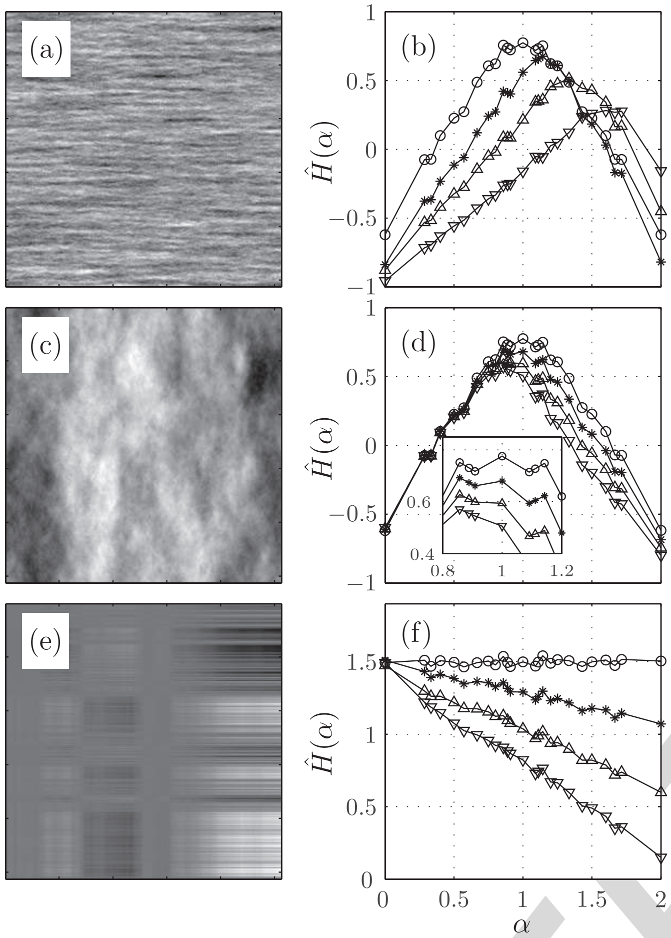

Fig. 8. **Other (an)isotropic selfsimilar Gaussian fields.** Left column, sample fields with $(H_1, H_2) = (0.2, 0.8)$ for **OSGRF** (top), **EFBF** (middle), **FBS** (bottom). Right column, $\hat{H}(\alpha)$ obtained for averages over 100 realizations, with $H_2 = 0.8$ and $H_1 = 0.8$ (∘), 0.6 (⋆), 0.4 (△) and 0.2 (▽). $\hat{H}(\alpha)$ clearly shows a maximum for $\alpha \neq 1$ when fields are anisotropic.

B. Testing Anisotropy

The estimation and test procedures described above were applied to these three classes of fields, for various setting of $[H_1, H_2]$. Estimated function $\hat{H}(\alpha)$, averaged over 100 realizations (size $2^{10} \times 2^{10}$), are reported in Fig. 8, right column. Isotropy rejection rates, obtained from $R = 100$ bootstrap surrogates for each of the 100 realizations, are reported in Table II.

For the three classes of fields, when $H_1 \neq H_2$, it is observed that $\hat{H}(\alpha)$ has a maximum for α that clearly departs from 1 and simultaneously that the isotropy rejection rates are far larger than the chosen $1 - \delta = 10\%$ significance level of the test. This is the case even for as small discrepancies between H_1 and H_2, as $H_2 - H_1 = 0.2$. These results clearly show that the proposed procedures clearly *detect* anisotropy.

For **EFBF**, it is reported in [46] that the test anisotropy proposed therein failed to detect anisotropy (i.e., test reject in 0% of cases), when $H_1 = 0.5$ and $H_2 = 0.7$. Trying as careful a comparison as possible, using the same model and parameter setting, it is found that the bootstrap test described in Section IV-C, yields rejection of isotropy, with the $1 - \delta = 10\%$ significance level, in 42% of cases, hence showing a much improved power (cf. Table II).

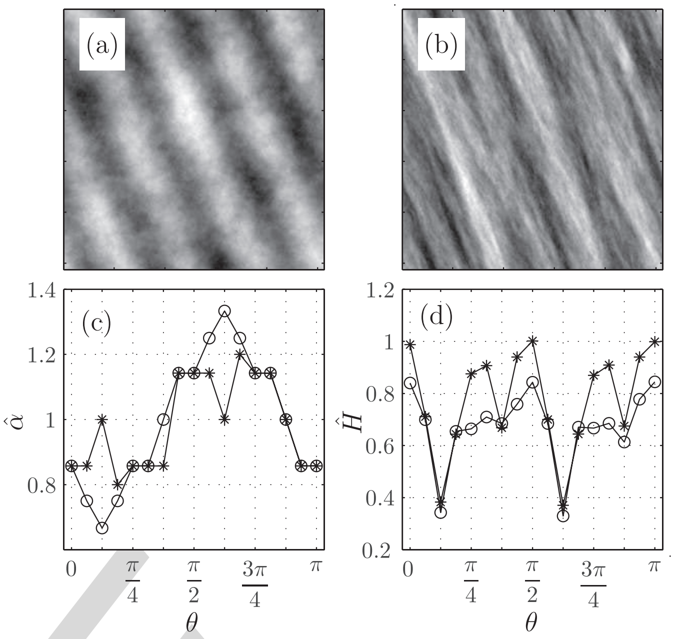

Fig. 9. (a) Isotropic self similar field ($\theta_0 = 0$, $H_0 = 0.5$, $\alpha_0 = 1$) to which a sine wave is superimposed along direction $\pi/8$; (b) Anisotropic self-similar fields with ($\theta_0 = \pi/8$, $H_0 = 0.5$, $\alpha_0 = 0.6$). $\hat{\alpha}$ (c) and $\hat{H}$ (d) as function of the angle analysis θ. The symbols (⋆) denote the results obtained for the field in (a) and the (∘) for the field in (b).

Conversely, for $H_1 = H_2$, it is observed for **EFBF** and **OSGRF** that $\hat{H}(\alpha)$ has a maximum for $\alpha = 1$ and simultaneously that the isotropy rejection rates reproduces the targeted significance level, hence confirming that these fields are isotropic. For **FBS**, $\hat{H}(\alpha)$ remains flat for all αs, while the rejection rates are higher than the targeted significance level, this is thus questioning isotropy of **FBS**, even when $H_1 = H_2$, a theoretically open issue.

C. Anisotropic Field With Superimposed Regular Texture

To finish, let us come back to the original issue disentangling self-similar with a true built-in anisotropy from isotropic selfsimilar processes to which an unrelated anisotropic texture is additively superimposed. To address this issue, let us compare a truly isotropic **OSGRF** $X_{\theta_0=0,\alpha_0=1,H_0=0.5}$, as defined in Eq. (2), to which a sine waveform trend, with orientation $\pi/8$ is additively superimposed (Fig. 9-a) to a truly anisotropic **OSGRF** $X_{\theta_0=\pi/8,\alpha_0=0.6,H_0=0.5}$. The estimation and test procedures described above are applied to 100 realizations of both fields, and $\hat{\alpha}(\theta)$ and $H(\theta)$ are displayed in Fig. 9c and d, respectively. For the truly anisotropic field (∘), $\hat{\alpha}(\theta)$ displays a visible minimum for $\hat{\theta} = \theta_0$, with estimated anisotropy ($\hat{\alpha} = \alpha(\hat{\theta}) = 0.66$) and selfsimilarity ($\hat{H}(\hat{\theta}) = 0.36$) parameters in satisfactory agreement with the true ones (∘ in 9d). This is thus suggesting a possible anisotropy. For the isotropic field, to which the directional sine wave trend has been additively superimposed, $\alpha(\theta)$ shows no clear minimum and instead a rather constant behavior in θ is observed, thus leading to conclude that anisotropy, clearly visible by eye on the sample field, is superimposed to rather than built within self-similarity.

This example suggests encouragingly that the proposed procedure can serve to analyze self-similarity in presence of anisotropy and may also help to disentangle self-similarity with built-in anisotropy from isotropic self-similarity with additively superimposed unrelated anisotropic trends.

VI. CONCLUSION

The present contribution aimed at studying images or fields where self-similarity is potentially tied to anisotropy. Replacing the standard 2D-DWT with the HWT, thus permitting to use different dilation factors along horizontal and vertical directions, enabled us first to estimate the rotation and anisotropy parameters. In turn, this permitted a correct estimation of the self-similarity parameter along the estimated anisotropy direction. This direction selection would not be permitted by the use of the sole 2D-DWT coefficients and thus constitutes the major benefits of the use of the HWT, and therefore the key feature of the present contribution.

Additionally, bootstrap based procedures, performed in the HWT coefficient domain, supply confidence intervals for the estimates and an isotropy test, that can be applied to a single image.

Though studied in depth for a specific Gaussian self-similar model, the proposed analysis is shown to enable the detection of anisotropy for a large variety of classes of Gaussian self-similar fields. Also, the proposed procedure can be used to help discriminating between self-similarity with true built-in anisotropy and isotropic self-similarity to which an anisotropic trend is added, this will be further investigated.

Extensions of the applicability of the present method or further developments geared towards the analysis of more general classes of fields modeling. Textures with scale invariance, that are not necessarily exactly self-similar and that may, weakly or significantly, depart from Gaussian distributions, are under current investigations. Notably, this study paves the way toward the far more difficult topic of multifractal analysis and formalim in presence of anisotropy, to which future efforts will be devoted.

MATLAB routines, designed by ourselves, implementing field synthesis and parameter estimation and test will be made publicly available at the time of publication.

REFERENCES

[1] S. G. Roux, A. Arneodo, and N. Decoster, "A wavelet-based method for multifractal image analysis. III. Applications to high-resolution satellite images of cloud structure," *Eur. Phys. J. B*, vol. 15, no. 4, pp. 765–786, Jun. 2000.

[2] P. Frankhauser, "L'approche fractale: Un nouvel outil dans l'analyse spatiale des agglomerations urbaines," *Population*, vol. 4, pp. 1005–1040, Jul./Aug. 1997.

[3] T. Lundahl, W. J. Ohley, S. M. Kay, and R. Siffert, "Fractional brownian motion: A maximum likelihood estimator and its application to image textures," *IEEE Trans. Med. Imaging*, vol. 5, no. 3, pp. 152–161, Sep. 1986.

[4] P. Kestener, J.-M. Lina, P. Saint-Jean, and A. Arneodo, "Wavelet-based multifractal formalism to assist in diagnosis in digitized mammograms," *Image Anal. Stereol.*, vol. 20, no. 3, pp. 169–174, 2001.

[5] M. Rachidi, F. Richard, H. Bierme, C. Roux, P. Fardellone, E. Lespessailles, C. Chappard, and C. Benhamou, "Osteoporosis risk assessment: A composite index combining clinical risk factors and biophysical parameters," *J. Bone Mineral Res.*, vol. 23, pp. S112–S112, Sep. 2008.

[6] F. Richard and H. Bierme, "Statistical tests of anisotropy for fractional brownian textures. application to full-field digital mammography," *J. Math. Imaging Vis.*, vol. 36, no. 3, pp. 227–240, Mar. 2010.

[7] M. Bergounioux and L. Piffet, "A second-order model for image denoising," *Set Valued Variat. Anal.*, vol. 18, nos. 3–4, pp. 277–306, Dec. 2010.

[8] D. Schertzer and S. Lovejoy, "Physically based rain and cloud modeling by anisotropic, multiplicative turbulent cascades," *J. Geophys. Res.*, vol. 92, no. 8, pp. 9693–9714, Aug. 1987.

[9] P. Abry, J. Stéphane, and H. Wendt, "When Van Gogh meets Mandelbrot: Multifractal classification of painting's textures," *Signal Process.*, vol. 93, no. 3, pp. 554–572, Mar. 2012.

[10] M. Unser, "Texture classification and segmentation using wavelet frames," *IEEE Trans. Image Process.*, vol. 4, no. 11, pp. 1549–1560, Nov. 1995.

[11] M. Nielsen, L. K. Hansen, P. Johansen, and J. Sporring, "Guest editorial: Special issue on statistics of shapes and textures," *J. Math. Imaging Vis.*, vol. 17, no. 2, p. 87, Sep. 2002.

[12] M. Do and M. Vetterli, "Wavelet-based texture retrieval using generalized Gaussian density and Kullback-Leibler distance," *IEEE Trans. Image Process.*, vol. 11, no. 2, pp. 146–158, Feb. 2002.

[13] M. Chantler and L. Van Gool, "Special issue on texture analysis and synthesis," *Int. J. Comput. Vis.*, vol. 62, nos. 1–2, pp. 1–5, Apr. 2005.

[14] G. Van de Wouwer, P. Scheunders, and D. Van Dyck, "Statistical texture characterization from discrete wavelet representations," *IEEE Trans. Image Processing*, vol. 8, no. 4, pp. 592–598, Apr. 1999.

[15] S. Peleg, J. Naor, R. Hartley, and D. Avnir, "Multiple resolution texture analysis and classification," *IEEE Trans. Pattern Anal. Mach. Intell.*, vol. 6, no. 4, pp. 518–523, Jul. 1984.

[16] L. M. Kaplan, "Extended fractal analysis for texture classification and segmentation," *IEEE Trans. Image Process.*, vol. 8, no. 11, pp. 1572–1585, Nov. 1999.

[17] B. Pesquet-Popescu and J. L. Vehel, "Stochastic fractal models for image processing," *IEEE Signal Process. Mag.*, vol. 19, no. 5, pp. 48–62, Sep. 2002.

[18] A. Bonami and A. Estrade, "Anisotropic analysis of some gaussian models," *J. Fourier Anal. Appl.*, vol. 9, no. 3, pp. 215–236, May 2003.

[19] H. Biermé, M. Meerschaert, and H. Scheffler, "Operator scaling stable random fields," *Stochastic Process. Appl.*, vol. 117, no. 3, pp. 312–332, Mar. 2007.

[20] A. R. Rao and R. C. Jain, "Computerized flow field analysis: Oriented texture fields," *IEEE Trans. Pattern Anal. Mach. Intell.*, vol. 14, no. 7, pp. 693–709, Jul. 1992.

[21] C. F. Shu and R. C. Jain, "Vector field analysis for oriented patterns," *IEEE Trans. Pattern Anal. Mach. Intell.*, vol. 16, no. 9, pp. 946–950, Sep. 1994.

[22] S. Roux, M. Clausel, B. Vedel, S. Jaffard, and P. Abry, "Transformé hyperbolique en ondelettes 2D pour la caractérisation d'images autosimilaires anisotropes," in *Proc. 23rd Colloq. Traitement Signal Images GRETSI*, Sep. 2011.

[23] R. A. DeVore, S. V. Konyagin, and V. N. Temlyakov, "Hyperbolic wavelet approximation," *Constructive Approximation*, vol. 14, no. 1, pp. 1–26, Jan. 1998.

[24] P. H. Westerink, "Subband coding of images," Ph.D. dissertation, Delft Univ. Technol., Delft, The Netherlands, 1989. AQ:2

[25] C. P. Rosiene and T. Q. Nguyen, "Tensor-product wavelet vs. Mallat decomposition: A comparative analysis," in *Proc. IEEE ISCAS*, vol. 3. Jul. 1999, pp. 431–434.

[26] T. P. Yu, A. Stoschek, and D. L. Donoho, "Translation- and direction-invariant denoising of 2D and 3D images: Experience and algorithms," *Proc. SPIE*, vol. 2825, p. 608, Oct. 1996. AQ:3

[27] V. Zavadsky, "Image approximation by rectangular wavelet transform," *J. Math. Imaging Vis.*, vol. 27, no. 2, pp. 129–138, Feb. 2007.

[28] L. Jacques, L. Duval, C. Chaux, and G. Peyre, "A panorama on multiscale geometric representations, intertwining spatial, directional and frequency selectivity," *Signal Process.*, vol. 91, no. 12, pp. 2699–2730, Dec. 2011.

[29] I. W. Selesnick, R. G. Baraniuk, and N. C. Kingsbury, "The dual-tree complex wavelet transform," *IEEE Signal Process. Mag.*, vol. 22, no. 6, pp. 123–151, Nov. 2005.

[30] H. Wendt, P. Abry, and S. Jaffard, "Bootstrap for empirical multifractal analysis," *IEEE Signal Process. Mag.*, vol. 24, no. 4, pp. 38–48, Jul. 2007.

[31] S. Mallat, *A Wavelet Tour of Signal Processing*. San Diego, CA, USA: Academic, 1998.

[32] H. Triebel, "Theory of functions spaces III," in *Birkhäuser Mathematics*. New York, NY, USA: Springer-Verlag, 2006.

[33] E. Bacry, J. Muzy, and A. Arneodo, "Singularity spectrum of fractal signals from wavelet analysis: Exact results," *J. Stat. Phys.*, vol. 70, nos. 3–4, pp. 635–674, Feb. 1993.

[34] I. Daubechies, *Ten Lectures on Wavelets*. Philadelphia, PA, USA: SIAM, 1992.

[35] M. Clausel and B. Vedel, *An Optimality Results About Sample Path Properties of Operator Scaling Gaussian Random Fields*. Cambridge, U.K.: Cambridge Univ. Press, Feb. 2013.

[36] P. Abry, M. Clausel, S. Jaffard, S. Roux, and B. Vedel, *Hyperbolic Wavelet Transform: An Efficient Tool for Multifractal Analysis of Anisotropic Textures*. Cambridge, U.K.: Cambridge Univ. Press, Oct. 2012.

[37] M. Clausel and B. Vedel, "Explicit constructions of operator scaling self-similar random gaussian fields," *Fractals*, vol. 19, no. 1, pp. 101–111, 2011.

[38] P. Abry, R. Baraniuk, P. Flandrin, R. Riedi, and D. Veitch, "Multiscale network traffic analysis, modeling, and inference using wavelets, multifractals, and cascades," *IEEE Signal Process. Mag.*, vol. 3, no. 19, pp. 28–46, May 2002.

[39] D. Veitch and P. Abry, "A statistical test for the time constancy of scaling exponents," *IEEE Trans. Signal Process.*, vol. 49, no. 10, pp. 2325–2334, Oct. 2001.

[40] D. Veitch and P. Abry, "A wavelet based joint estimator of the parameters of long-range dependence," *IEEE Trans. Inf. Theory*, vol. 45, no. 3, pp. 878–897, Apr. 1999.

[41] H. Wendt and P. Abry, "Multifractality tests using bootstrapped wavelet leaders," *IEEE Trans. Signal Process.*, vol. 55, no. 10, pp. 4811–4820, Oct. 2007.

[42] H. Wendt and P. Abry, "Bootstrap tests for the time constancy of multifractal attributes," in *Proc. IEEE ICASSP*, vols. 1–12. Apr. 2008, pp. 3465–3468.

[43] H. Wendt, S. Roux, S. Jaffard, and P. Abry, "Wavelet leaders and bootstrap for multifractal analysis of images," *Signal Process.*, vol. 89, no. 6, pp. 1100–1114, Jun. 2009.

[44] B. Efron, *The Jackknife, the Bootstrap and Other Resampling Plans*. Philadelphia, PA, USA: SIAM, 1982.

[45] P. Hall, *The Bootstrap and Edgeworth Expansion*. New York, NY, USA: Springer-Verlag, 1992.

[46] H. Biermé and F. Richard, "Analysis of texture anisotropy based on some gaussian fields with spectral density," in *Mathematical Image Processing* (Springer Proceedings in Mathematics), M. Bergounioux, Ed. New York, NY, USA: Springer-Verlag, 2011, pp. 59–73.

[47] A. Kamont, "On the fractional anisotropic Wiener field," *Probab. Math. Stat.*, vol. 16, no. 1, pp. 85–98, 1996.

[48] A. Ayache, S. Léger, and M. Pontier, "Drap brownien fractionnaire," *Potential Anal.*, vol. 17, no. 1, pp. 31–43, 2002.

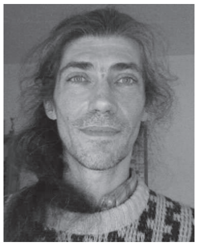

Stéphane G. Roux was born in Montpellier, France, in 1967. He received the Degree from the University of Montpellier, Montpellier, France, and the Ph.D. degree in physics from the University of Aix-Marseille, Aix-Marseille, France, in 1996. Since September 2001, he has been an Associate Professor with the Laboratoire de Physique of Ecole Normale Supérieure de Lyon, Lyon, France. His current research interests include scale invariance, wavelet analysis, and their practical applications in physics.

Marianne Clausel was born in Marseille, France, in 1974. She received the Degree of Professeur–Agrégée, in 1999, and the Ph.D. degree in applied mathematics from Paris–Est Créteil University, Paris, France, in 2008. Since September 2011, she has been an Assistant Professor with the Laboratoire Jean Kuntzmann, Grenoble Alpes University, Grenoble, France. She received a five years grant from chaire CNRS–UJF from 2011 to 2016. Her current research interests include wavelet-based analysis of textures and modeling of the dependence of time series or spatial datas (long–range dependence, copulas).

Béatrice Vedel was born in Compiègne, France, in 1978. She received the Degree from Université de Picardie Jules Verne, Beauvais, France, in 2001, and the Ph.D. degree in mathematics in 2004. Since September 2008, she has been an Associate Professor with the Laboratoire de Mathématiques de Bretagne Atlantique, Université de Bretagne Sud, Lorient, France. Her current research interests include functional analysis, wavelet analysis, multifractals, and image processing.

Stéphane Jaffard was born in Boulogne-Billancourt, France, in 1962. He received the Degree from Ecole Polytechnique, Lausanne, Switzerland, in 1984, and the Ph.D. degree in mathematics, in 1989, under the supervision of Y. Meyer. Since September 1995, he has been a Professor with the University Paris Est at Créteil, Paris, France. He was a member of the Institut Universitaire de France, France, from 2000 to 2005. He is the co-author of *Wavelets: Tools for Science and Technology* (SIAM, 2001) with Y. Meyer and R. Ryan. He is an Editorial Board Member of the *Applied and Computational Harmonic Analysis*, the *Journal of Fourier Analysis and its Applications*, and the *Constructive Approximation, Applied and Numerical Harmonic Analysis*. His current research interests include Fourier series, wavelet analysis, pointwise smoothness, multifractals, and stochastic processes. He is currently the Head of the Bézout LabEx.

Patrice Abry (F'11) was born in Bourg-en-Bresse, France, in 1966. He received the Degree of Professeur Agrégé de Sciences Physiques from Ecole Normale Supérieure de Cachan, Cachan, France, in 1989, and the Ph.D. degree in physics and signal processing from Ecole Normale Supérieure de Lyon, Lyon, France, and the Université Claude-Bernard Lyon I, Lyon, in 1994. Since October 1995, he has been a Permanent CNRS Researcher with the Laboratoire de Physique of Ecole Normale Supérieure de Lyon. He received the AFCET-MESR-CNRS prize for best Ph.D. in signal processing from 1993 to 1994. He is the author of *Ondelettes et Turbulences—Multirésolution, algorithmes de décompositions, invariance d'échelle et signaux de pression* (Diderot, 1997). He is the co-editor of *Scaling, Fractals and Wavelets*. His current research interests include wavelet-based analysis, modeling of scaling phenomena, and related topics (self-similarity, stable processes, multi-fractal, 1/f processes, long-range dependence, local regularity of processes, infinitely divisible cascades, departures from exact scale invariance). He shows a strong interest in real-world applications, ranging from hydrodynamic turbulence to the analysis and modeling of computer network teletraffic. He was involved in the study of heart rate variability for both adults and fetuses, in collaboration with French academic hospitals.

AUTHOR QUERIES

AQ:1 = Please provide callout descriptions in the captions for all lettered parts of Figs. 3, 4, and 8.
AQ:2 = Please provide the department name for ref. [24].
AQ:3 = Please confirm the volume no for ref. [26].